



Analytical model for measurement of through-thickness axisymmetric radial residual stress

Huan Liu, Lu Deng*, YuLong He

Key Laboratory for Damage Diagnosis of Engineering Structures of Hunan Province, Hunan University, Changsha, 410082, China

ARTICLE INFO

Keywords:

Through-thickness
Radial residual stress
Hole drilling
Analytical solution
Stress measurement

ABSTRACT

In this study, an analytical model is proposed to measure the through-thickness axisymmetric radial residual stress. Firstly, the rigorous analytical solution for the strain of a plate with a hole subjected to the through-thickness axisymmetric radial stress is found based on the general solution for a homogeneous isotropic elastic solid. It is assumed that the through-thickness axisymmetric radial residual stress can be expanded into the Maclaurin series. Then, the reverse procedure is proposed to determine the coefficients of the series by minimizing the predicted and measured surface radial strains with hole drilling. The proposed model is validated by finite element method (FEM) for a few typical distribution types. The influence of individual terms of the series on the surface radial strain is investigated, and the results show that the high order term results in a small strain value. The model is able to predict the residual stresses by peening as well as those with linear, bi-linear, quad-linear, and sinusoidal distributions. Moreover, a method to measure the resultant force and moment per unit hole circumference is proposed.

1. Introduction

Residual stresses are generated in the material manufacture process, due to uneven deformation resulted from inhomogeneous heating, phase change, and plastic deformation. Residual stresses have significant practical implications for the component performance, including stiffness, stability, fracture, and fatigue [1–4]. Therefore, many studies have been conducted to evaluate the residual stresses of workpieces in the research field of manufacturing.

The techniques used for residual stress measurement can be categorized into destructive and non-destructive methods according to the different measurement principles. For destructive methods, the residual stress is evaluated by monitoring the mechanical strain relaxation [5] through the principle of elastic mechanics. There are several classic destructive methods including the hole drilling, sectioning, and ring-core. Since the hole drilling method is relatively simple, semi-destructive, and economical, it has become one of the most common destructive methods [6–8]. The American Society for Testing Materials (ASTM) issued a standard for the hole drilling method [9]. From the standard, the residual stress in a finite depth can be measured by the incremental hole drilling method. However, the released interior strain by the hole drilling is relatively small and FEM is needed to determine the calibrated coefficients [10]. In order to improve the measuring accuracy, the ring-core method was developed with an increased strain release in the middle of the ring-core region [11]. Nevertheless, it is

more destructive and less convenient for practical implementation. To determine the residual stress along the thickness, the sectioning method comprised of longitudinal sectioning and transversal sectioning was established, which is suitable for uniaxial stress measurement [12–14]. However, this method only gives the average stress in the thickness range and is fully destructive.

To prevent the material from being damaged, non-destructive testing methods were developed, including X-ray diffraction method (XRD), neutron diffraction method, ultrasonic method, et al. XRD is one of the most widely used non-destructive methods. Based on the Bragg equation, the residual stress is calculated by measuring the lattice strain. Although XRD can provide high precision and localized characteristics of measurements, the measured residual stress is limited to the surface residual stress [15–17]. Compared with XRD, neutron diffraction has better penetration ability but the instrument is very expensive [18]. Based on the phenomenon of acoustic birefringence, the ultrasonic method is applicable to measuring the residual stress inside the material but it is sensitive to the microstructures and defects [3].

It can be seen that a lot of efforts have been spent on measuring the through-thickness residual stress. Nowadays, a thin layer removal technique is often used to expose the interior of the material for applying the available measurement methods [19,20]. However, the removal procedure may be time-consuming and the variation of the

* Corresponding author.

E-mail addresses: liuhuan92@hnu.edu.cn (H. Liu), denglu@hnu.edu.cn (L. Deng), heyil@hnu.edu.cn (Y. He).

residual stress on the layer thickness is still unknown. It is necessary to develop a measurement method with high efficiency, accuracy, and low cost. Owing to the development of non-contact displacement measurement methods, optical alternatives to the use of strain gauges become possible [21]. The main optical alternatives include holographic interferometry [22,23], electronic speckle pattern interferometry [24,25], and DIC (digital image correlation) [26]. Subsequently, the measured surface strain field near the drilling hole may be utilized to evaluate the through-thickness residual stress.

The non-uniform residual stresses near the surface of a thick material can be measured using the hole-drilling strain gauge method [9]. The stress profile is assumed as a staircase shape and FEM is needed to determinate the calibration constants. However, this method may not be able to measure the stresses along the whole thickness of the plate. In this paper, an analytical model is developed to make it possible to measure the through-thickness axisymmetric radial residual stress with hole drilling. Firstly, the rigorous analytical solution is derived for the strain of a plate with a hole subjected to the through-thickness axisymmetric radial stress. Followed by the analytical solution, the reverse procedure is established to measure the stress by minimizing the predicted and measured surface radial strains. The surface radial strains at the specific locations can be obtained using DIC. The proposed model is validated by FEM for a few typical types of distribution. The measurements for the residual stresses by peening as well as those with linear, bi-linear, quad-linear, and sinusoidal distributions are discussed. Moreover, a method for measuring the resultant force and moment per unit hole circumference is proposed.

2. The model

Fig. 1 shows the geometry of the model, where a small hole with a diameter $2r_0$ is drilled in an infinite plate. The linear elastic, homogeneous, and isotropic plate has a thickness of $2h$, shear modulus of G , and Poisson's ratio of ν . The Cartesian coordinate system $xoyz$ and cylindrical coordinate system $ro\theta z$ are shown in Fig. 1. It is assumed that there are only axisymmetric residual stresses varying along the plate thickness.

DIC technique provides a good option for the measurement of full-field displacement by matching the subsets between the original and deformed images. Subsequently, the strain field is retrieved from the difference of the displacement vectors. DIC was applied to measure the surface strain field with hole drilling, and the maximum mean and standard deviation of the noise were estimated as -6.8 [$\mu\text{m}/\text{m}$] and 42.7 [$\mu\text{m}/\text{m}$], respectively [27]. The measured strain results are heavily affected by the parameters used in calculation, e.g., the subset size, the grid step, and the strain window size due to surface fitting functions. The trade-off between the low strain noise and better-resolved strain gradients can be achieved by selecting a proper strain window size [28]. Therefore, the surface radial strains at the given locations can be obtained according to the measured strain field after the hole drilling. The measured radial strains on the top and bottom surfaces of the plate are denoted by ε_{mt} and ε_{mb} , respectively. Since there are no stresses on the hole, the strains ε_{mt} and ε_{mb} are considered to be introduced by the axisymmetric radial stress $\sigma_{r_0}(z)$, which has the same magnitude but opposite direction to the original axisymmetric radial residual stress. The relationship between the axisymmetric radial stress $\sigma_{r_0}(z)$ and the surface radial strains needs to be established for the reverse procedure. Since the geometry and the stress boundary conditions are axisymmetric, the problem is an axisymmetric one.

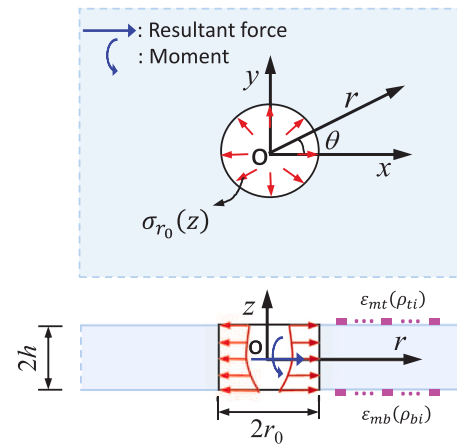


Fig. 1. The model for the measurement of the through-thickness axisymmetric radial residual stress.

Referring to the general solution for a homogeneous isotropic elastic solid mentioned by Green [29], the solutions for the current problem can be expressed as follows considering the axial symmetry.

Solution A

$$\begin{aligned} u_r &= \frac{\partial \varphi}{\partial r}, \quad u_z = \frac{\partial \varphi}{\partial z} \\ \frac{\sigma_z}{2G} &= \frac{\partial^2 \varphi}{\partial z^2}, \quad \frac{\tau_{rz}}{2G} = \frac{\partial^2 \varphi}{\partial r \partial z}, \quad \frac{\sigma_r}{2G} = \frac{\partial^2 \varphi}{\partial r^2} \\ \frac{\sigma_\theta}{2G} &= -\frac{\partial^2 \varphi}{\partial r^2} - \frac{\partial^2 \varphi}{\partial z^2} \end{aligned} \quad (1)$$

Solution B

$$\begin{aligned} u_r &= \eta \frac{\partial \phi}{\partial r} + 2z \frac{\partial^2 \phi}{\partial r \partial z}, \quad u_z = -\eta \frac{\partial \phi}{\partial z} + 2z \frac{\partial^2 \phi}{\partial z^2} \\ \frac{\sigma_z}{2G} &= -\frac{\partial^2 \phi}{\partial z^2} + 2z \frac{\partial^3 \phi}{\partial z^3}, \quad \frac{\tau_{rz}}{2G} = \frac{\partial^2 \phi}{\partial r \partial z} + 2z \frac{\partial^3 \phi}{\partial r \partial z^2} \\ \frac{\sigma_r}{2G} &= \eta \frac{\partial^2 \phi}{\partial r^2} + 2z \frac{\partial^3 \phi}{\partial r^2 \partial z} + (\eta - 3) \frac{\partial^2 \phi}{\partial z^2} \\ \frac{\sigma_\theta}{2G} &= -3 \frac{\partial^2 \phi}{\partial z^2} - 2z \frac{\partial^3 \phi}{\partial z^3} - \eta \frac{\partial^2 \phi}{\partial r^2} - 2z \frac{\partial^3 \phi}{\partial r^2 \partial z} \end{aligned} \quad (2)$$

Solution C

$$\begin{aligned} u_r &= 2r \frac{\partial^2 \chi}{\partial z^2} + (\eta + 5) \frac{\partial \chi}{\partial r}, \quad u_z = -2r \frac{\partial^2 \chi}{\partial r \partial z} + (3 - \eta) \frac{\partial \chi}{\partial z} \\ \frac{\sigma_z}{2G} &= -2r \frac{\partial^3 \chi}{\partial r \partial z^2}, \quad \frac{\tau_{rz}}{2G} = 3 \frac{\partial^2 \chi}{\partial r \partial z} + r \frac{\partial^3 \chi}{\partial z^3} - r \frac{\partial^3 \chi}{\partial r \partial z^2} \\ \frac{\sigma_r}{2G} &= (\eta + 5) \frac{\partial^2 \chi}{\partial r^2} + 2r \frac{\partial^3 \chi}{\partial r \partial z^2} + (\eta - 1) \frac{\partial^2 \chi}{\partial z^2} \\ \frac{\sigma_\theta}{2G} &= -(\eta + 5) \frac{\partial^2 \chi}{\partial r^2} - 6 \frac{\partial^2 \chi}{\partial z^2} \end{aligned} \quad (3)$$

where φ , ϕ , and χ are the potential functions; $\eta = 3 - 4\nu$.

Besides, the aforementioned potential functions φ , ϕ , and χ should satisfy Laplace's equation as

$$\left(\frac{1}{r} \frac{\partial}{\partial r} + \frac{\partial^2}{\partial r^2} + \frac{\partial^2}{\partial z^2} \right) (\varphi, \phi, \chi) = 0 \quad (4)$$

Since any function can be expressed by the superposition of the even functions and the odd functions, the solutions of the above potential functions can be decomposed into the even solutions and odd solutions that meet the boundary conditions on the top and bottom surfaces.

3. The analytical solution

3.1. The even solutions of the potential functions

For convenience, the following dimensionless parameters are introduced

$$\zeta = \frac{z}{h}, \quad \rho = \frac{r}{h}, \quad \rho_0 = \frac{r_0}{h} \tag{5}$$

Using the method of separation of variables for Eq. (4), one of the even solution for the function φ is

$$\varphi_{00} = K_0(\alpha_m \rho) \cos(\alpha_m \zeta), \quad \alpha_m = m\pi, \quad m = 1, 2, 3, \dots \tag{6}$$

where $K_0()$ is the modified Bessel function of zero order of the second kind.

According to Eq. (1), the shear stress τ_{rz} introduced by φ_{00} is zero on the surfaces of $\zeta = \pm 1$. The normal stress σ_z is

$$\frac{\sigma_z}{2G} = -\alpha_m^2 K_0(\alpha_m \rho) \cos(\alpha_m \zeta) \tag{7}$$

To cancel σ_z on the surfaces of $\zeta = \pm 1$ without introducing shear stress τ_{rz} on the surfaces, the solutions of the types B and C are found as

$$\varphi_{01} = \sum_{n=0,1,2,\dots}^{\infty} c_{mn0} P_0(u_n \rho) \cosh(u_n \zeta) \tag{8a}$$

$$\phi_{01} = \sum_{n=0,1,2,\dots}^{\infty} c_{mn1} P_0(u_n \rho) \cosh(u_n \zeta) \tag{8b}$$

where $P_0(u_n \rho)$ is defined as

$$P_0(u_n \rho) = J_0(u_n \rho) - \frac{J_1(u_n \rho)}{Y_1(u_n \rho)} Y_0(u_n \rho) \tag{9}$$

where $J_i()$ and $Y_i()$ are the Bessel functions of the i th order of the first kind and second kind, respectively.

The constant u_n in the above equation is the n th root of the following equation

$$J_0(u_n \rho_1) - \frac{J_1(u_n \rho_0)}{Y_1(u_n \rho_0)} Y_0(u_n \rho_1) = 0 \tag{10}$$

where ρ_1 is a constant much larger than ρ_0 .

The functions $P_0(u_n \rho)$ are orthogonal on the interval $[\rho_0, \rho_1]$ with the weight ρ . Hence, $K_0(\alpha_m \rho)$ and $\rho K_1(\alpha_m \rho)$ can be expressed by $P_0(u_n \rho)$ as

$$K_0(\alpha_m \rho) = \sum_{n=0,1,2,\dots}^{\infty} a_{mn} P_0(u_n \rho), \quad \rho K_1(\alpha_m \rho) = \sum_{n=0,1,2,\dots}^{\infty} b_{mn} P_0(u_n \rho) \tag{11}$$

where the constants a_{mn} and b_{mn} are

$$a_{mn} = \frac{2 [\rho_1 u_n K_0(\alpha_m \rho_1) P_1(u_n \rho_1) + \rho_0 \alpha_m K_1(\alpha_m \rho_0) P_0(u_n \rho_0)]}{(\alpha_m^2 + u_n^2) [\rho_1^2 P_1(u_n \rho_1)^2 - \rho_0^2 P_0(u_n \rho_0)^2]} \tag{12}$$

$$b_{mn} = \frac{4 [\rho_1 u_n \alpha_m K_0(\alpha_m \rho_1) P_1(u_n \rho_1) - \rho_0 u_n^2 K_1(\alpha_m \rho_0) P_0(u_n \rho_0)]}{(\alpha_m^2 + u_n^2) [\rho_1^2 P_1(u_n \rho_1)^2 - \rho_0^2 P_0(u_n \rho_0)^2]} + \frac{2 \rho_1^2 u_n K_1(\alpha_m \rho_1) P_1(u_n \rho_1) + 2 \rho_0 P_0(u_n \rho_0) [\rho_0 \alpha_m K_0(\alpha_m \rho_0) + 2 K_1(\alpha_m \rho_0)]}{(\alpha_m^2 + u_n^2) [\rho_1^2 P_1(u_n \rho_1)^2 - \rho_0^2 P_0(u_n \rho_0)^2]}$$

The constants c_{mn0} and c_{mn1} can be determined through the condition of zero stresses on the surfaces $\zeta = \pm 1$. From Eqs. (1), (2), (7), (8), and (11), the following can be obtained

$$c_{mn0} \sinh u_n + c_{mn1} (\sinh u_n + 2u_n \cosh u_n) = 0 \tag{13a}$$

$$c_{mn0} \cosh u_n + c_{mn1} (2u_n \sinh u_n - \cosh u_n) = (-1)^m \frac{\alpha_m^2}{u_n^2} a_{mn} \tag{13b}$$

Solving Eq. (13), gives

$$c_{mn0} = \frac{(-1)^m \alpha_m^2 a_{mn} (\sinh u_n + 2u_n \cosh u_n)}{u_n^2 (2u_n + \sinh 2u_n)}, \quad c_{mn1} = \frac{(-1)^{m+1} \alpha_m^2 a_{mn} \sinh u_n}{u_n^2 (2u_n + \sinh 2u_n)} \tag{14}$$

Therefore, the final forms for the functions φ and ϕ , which produce zero stresses on the surfaces are

$$\varphi_0 = K_0(\alpha_m \rho) \cos(\alpha_m \zeta) + \sum_{n=0,1,2,\dots}^{\infty} c_{mn0} P_0(u_n \rho) \cosh(u_n \zeta) \tag{15}$$

$$\phi_0 = \sum_{n=0,1,2,\dots}^{\infty} c_{mn1} P_0(u_n \rho) \cosh(u_n \zeta)$$

Similar to the solution for the functions φ_0 and ϕ_0 , another independent solution for the functions φ , ϕ , and χ is

$$\chi_1 = K_0(\alpha_m \rho) \cos(\alpha_m \zeta)$$

$$\varphi_1 = \sum_{n=0,1,2,\dots}^{\infty} d_{mn0} P_0(u_n \rho) \cosh(u_n \zeta) \tag{16}$$

$$\phi_1 = \sum_{n=0,1,2,\dots}^{\infty} d_{mn1} P_0(u_n \rho) \cosh(u_n \zeta)$$

where the constants d_{mn0} and d_{mn1} are

$$d_{mn0} = \frac{2(-1)^m \alpha_m^3 b_{mn} (\sinh u_n + 2u_n \cosh u_n)}{u_n^2 (2u_n + \sinh 2u_n)}, \tag{17}$$

$$d_{mn1} = \frac{2(-1)^{m+1} \alpha_m^3 b_{mn} \sinh u_n}{u_n^2 (2u_n + \sinh 2u_n)}$$

From Eqs. (15) and (16), it can be seen that when $m = 0$ the solutions are invalid. To establish the complete even solutions of the potential functions, the following functions φ_2 and ϕ_2 satisfying the boundary conditions are required

$$\varphi_2 = \phi_2 = \ln \rho \tag{18}$$

3.2. The odd solutions of the potential functions

One of the odd solution for the function φ satisfying Eq. (4) can be expressed by

$$\varphi_{00}^* = K_0(\beta_m \rho) \sin(\beta_m \zeta), \quad \beta_m = \frac{2m-1}{2} \pi, \quad m = 1, 2, 3, \dots \tag{19}$$

From Eq. (1), the shear stress τ_{rz} vanishes on the surfaces of $\zeta = \pm 1$. The normal stress σ_z is

$$\frac{\sigma_z}{2G} h^2 = -\beta_m^2 K_0(\beta_m \rho) \sin(\beta_m \zeta) \tag{20}$$

To cancel the normal stress without giving the shear stress on the surfaces $\zeta = \pm 1$, the following functions φ_{01}^* and ϕ_{01}^* are introduced

$$\varphi_{01}^* = \sum_{n=0,1,2,\dots}^{\infty} c_{mn0}^* P_0(u_n \rho) \sinh(u_n \zeta) \tag{21}$$

$$\phi_{01}^* = \sum_{n=0,1,2,\dots}^{\infty} c_{mn1}^* P_0(u_n \rho) \sinh(u_n \zeta)$$

Similar to Eq. (11), $K_0(\beta_m \rho)$ and $\rho K_1(\beta_m \rho)$ can be expressed by $P_0(u_n \rho)$ as

$$K_0(\beta_m \rho) = \sum_{n=0,1,2,\dots}^{\infty} a_{mn}^* P_0(u_n \rho), \quad \rho K_1(\beta_m \rho) = \sum_{n=0,1,2,\dots}^{\infty} b_{mn}^* P_0(u_n \rho) \tag{22}$$

where the constants a_{mn}^* and b_{mn}^* can be obtained by replacing α_m with β_m in the expressions of a_{mn} and b_{mn} in Eq. (12), respectively.

The constants c_{mn0}^* and c_{mn1}^* can be obtained by the condition of zero stresses on the surfaces of $\zeta = \pm 1$. From Eqs. (1), (2), (20), (21) and

(22), the following can be obtained

$$c_{mn0}^* \cosh u_n + c_{mn1}^* (\cosh u_n + 2u_n \sinh u_n) = 0 \tag{23a}$$

$$c_{mn0}^* \sinh u_n + c_{mn1}^* (2u_n \cosh u_n - \sinh u_n) = (-1)^{m+1} \frac{\beta_m^2}{u_n^2} a_{mn}^* \tag{23b}$$

Therefore, c_{mn0}^* and c_{mn1}^* are

$$c_{mn0}^* = \frac{(-1)^{m+1} \beta_m^2 a_{mn}^* (\cosh u_n + 2u_n \sinh u_n)}{u_n^2 (\sinh 2u_n - 2u_n)}, \quad c_{mn1}^* = \frac{(-1)^m \beta_m^2 a_{mn}^* \cosh u_n}{u_n^2 (\sinh 2u_n - 2u_n)} \tag{24}$$

To sum up, the functions φ_0^* and ϕ_0^* , which satisfy the boundary conditions, are

$$\begin{aligned} \varphi_0^* &= K_0(\beta_m \rho) \sin(\beta_m \zeta) + \sum_{n=0,1,2,\dots} c_{mn0}^* P_0(u_n \rho) \sinh(u_n \zeta) \\ \phi_0^* &= \sum_{n=0,1,2,\dots} c_{mn1}^* P_0(u_n \rho) \sinh(u_n \zeta) \end{aligned} \tag{25}$$

With similar derivation to the functions φ_0^* and ϕ_0^* , the other independent odd solution for the functions φ , ϕ , and χ is

$$\begin{aligned} \chi_1^* &= K_0(\beta_m \rho) \sin(\beta_m \zeta) \\ \varphi_1^* &= \sum_{n=0,1,2,\dots} d_{mn0}^* P_0(u_n \rho) \sinh(u_n \zeta) \\ \phi_1^* &= \sum_{n=0,1,2,\dots} d_{mn1}^* P_0(u_n \rho) \sinh(u_n \zeta) \end{aligned} \tag{26}$$

where the constants d_{mn0}^* and d_{mn1}^* are

$$\begin{aligned} d_{mn0}^* &= \frac{2(-1)^{m+1} \beta_m^3 b_{mn}^* (\cosh u_n + 2u_n \sinh u_n)}{u_n^2 (\sinh 2u_n - 2u_n)}, \\ d_{mn1}^* &= \frac{2(-1)^m \beta_m^3 b_{mn}^* \cosh u_n}{u_n^2 (\sinh 2u_n - 2u_n)} \end{aligned} \tag{27}$$

3.3. The stresses

Once the potential functions are determined, the stresses can be calculated by Eqs. (1)~(3). The stresses $\sigma_{r0}(m, \rho, \zeta)$, $\tau_{rz0}(m, \rho, \zeta)$, and $\sigma_{\theta 0}(m, \rho, \zeta)$ corresponding to the functions φ_0 and ϕ_0 are

$$\begin{aligned} \frac{\sigma_{r0}}{2G} h^2 &= \omega_{m0} \cos(\alpha_m \zeta) + \sum_{n=0,1,2,\dots} e_{mn0} \cosh(u_n \zeta) + \sum_{n=0,1,2,\dots} e_{mn1} \zeta \sinh(u_n \zeta) \\ \frac{\tau_{rz0}}{2G} h^2 &= \omega_{m1} \sin(\alpha_m \zeta) + \sum_{n=0,1,2,\dots} e_{mn2} \sinh(u_n \zeta) + \sum_{n=0,1,2,\dots} e_{mn3} \zeta \cosh(u_n \zeta) \\ \frac{\sigma_{\theta 0}}{2G} h^2 &= \omega_{m2} \cos(\alpha_m \zeta) + \sum_{n=0,1,2,\dots} e_{mn4} \cosh(u_n \zeta) + \sum_{n=0,1,2,\dots} e_{mn5} \zeta \sinh(u_n \zeta) \end{aligned} \tag{28}$$

where $\omega_{m0} \sim \omega_{m2}$ and $e_{mn0} \sim e_{mn5}$ are listed in Appendix.

The stresses $\sigma_{r1}(m, \rho, \zeta)$, $\tau_{rz1}(m, \rho, \zeta)$, and $\sigma_{\theta 1}(m, \rho, \zeta)$ corresponding to the functions χ_1 , φ_1 , and ϕ_1 are

$$\begin{aligned} \frac{\sigma_{r1}}{2G} h^2 &= \lambda_{m0} \cos(\alpha_m \zeta) + \sum_{n=0,1,2,\dots} f_{mn0} \cosh(u_n \zeta) + \sum_{n=0,1,2,\dots} f_{mn1} \zeta \sinh(u_n \zeta) \\ \frac{\tau_{rz1}}{2G} h^2 &= \lambda_{m1} \sin(\alpha_m \zeta) + \sum_{n=0,1,2,\dots} f_{mn2} \sinh(u_n \zeta) + \sum_{n=0,1,2,\dots} f_{mn3} \zeta \cosh(u_n \zeta) \\ \frac{\sigma_{\theta 1}}{2G} h^2 &= \lambda_{m2} \cos(\alpha_m \zeta) + \sum_{n=0,1,2,\dots} f_{mn4} \cosh(u_n \zeta) + \sum_{n=0,1,2,\dots} f_{mn5} \zeta \sinh(u_n \zeta) \end{aligned} \tag{29}$$

where $\lambda_{m0} \sim \lambda_{m2}$ and $f_{mn0} \sim f_{mn5}$ are listed in Appendix.

The stresses $\sigma_{r2}(m, \rho, \zeta)$, $\tau_{rz2}(m, \rho, \zeta)$, and $\sigma_{\theta 2}(m, \rho, \zeta)$ corresponding to the functions ϕ_2 and χ_2 are the plane stress solution as

$$\begin{aligned} \frac{\sigma_{r2}}{2G} h^2 &= -(\eta + 6) \frac{1}{\rho^2} \\ \frac{\tau_{rz2}}{2G} h^2 &= 0 \\ \frac{\sigma_{\theta 2}}{2G} h^2 &= (\eta + 6) \frac{1}{\rho^2} \end{aligned} \tag{30}$$

Similar to the stresses given by the even potential functions, the stresses $\sigma_{r0}^*(m, \rho, \zeta)$, $\tau_{rz0}^*(m, \rho, \zeta)$, and $\sigma_{\theta 0}^*(m, \rho, \zeta)$ corresponding to the functions φ_0^* and ϕ_0^* are

$$\begin{aligned} \frac{\sigma_{r0}^*}{2G} h^2 &= \omega_{m0}^* \sin(\beta_m \zeta) + \sum_{n=0,1,2,\dots} e_{mn0}^* \sinh(u_n \zeta) + \sum_{n=0,1,2,\dots} e_{mn1}^* \zeta \cosh(u_n \zeta) \\ \frac{\tau_{rz0}^*}{2G} h^2 &= \omega_{m1}^* \cos(\beta_m \zeta) + \sum_{n=0,1,2,\dots} e_{mn2}^* \cosh(u_n \zeta) + \sum_{n=0,1,2,\dots} e_{mn3}^* \zeta \sinh(u_n \zeta) \\ \frac{\sigma_{\theta 0}^*}{2G} h^2 &= \omega_{m2}^* \sin(\beta_m \zeta) + \sum_{n=0,1,2,\dots} e_{mn4}^* \sinh(u_n \zeta) + \sum_{n=0,1,2,\dots} e_{mn5}^* \zeta \cosh(u_n \zeta) \end{aligned} \tag{31}$$

where the coefficients ω_{m0}^* , ω_{m2}^* , e_{mn0}^* , e_{mn1}^* , ..., e_{mn4}^* can be obtained by replacing α_m with β_m , c_{mn0} with c_{mn0}^* , and c_{mn1} with c_{mn1}^* in Eq. (A.1); $\omega_{m1}^* = -\beta_m^2 K_1(\beta_m \rho)$.

The stresses $\sigma_{r1}^*(m, \rho, \zeta)$, $\tau_{rz1}^*(m, \rho, \zeta)$, and $\sigma_{\theta 1}^*(m, \rho, \zeta)$ given by the functions χ_1^* , φ_1^* , and ϕ_1^* are

$$\begin{aligned} \frac{\sigma_{r1}^*}{2G} h^2 &= \lambda_{m0}^* \sin(\beta_m \zeta) + \sum_{n=0,1,2,\dots} f_{mn0}^* \sinh(u_n \zeta) + \sum_{n=0,1,2,\dots} f_{mn1}^* \zeta \cosh(u_n \zeta) \\ \frac{\tau_{rz1}^*}{2G} h^2 &= \lambda_{m1}^* \cos(\beta_m \zeta) + \sum_{n=0,1,2,\dots} f_{mn2}^* \cosh(u_n \zeta) + \sum_{n=0,1,2,\dots} f_{mn3}^* \zeta \sinh(u_n \zeta) \\ \frac{\sigma_{\theta 1}^*}{2G} h^2 &= \lambda_{m2}^* \sin(\beta_m \zeta) + \sum_{n=0,1,2,\dots} f_{mn4}^* \sinh(u_n \zeta) + \sum_{n=0,1,2,\dots} f_{mn5}^* \zeta \cosh(u_n \zeta) \end{aligned} \tag{32}$$

where the coefficients λ_{m0}^* , λ_{m2}^* , f_{mn0}^* , f_{mn1}^* , ..., f_{mn4}^* can be found by replacing α_m with β_m , d_{mn0} with d_{mn0}^* , and d_{mn1} with d_{mn1}^* in Eq. (A.2); $\lambda_{m1}^* = -2\beta_m^3 \rho K_0(\beta_m \rho) - 4\beta_m^2 K_1(\beta_m \rho)$.

It is beneficial to represent these stresses by the Fourier expansions in the coordinate ζ . The required forms can be obtained by using the following Fourier expansions

$$\begin{aligned} \cosh(u_n \zeta) &= \sum_{m=1,2,\dots} X_{mn0} \cos(\alpha_m \zeta) + X_{n0}, \\ \zeta \sinh(u_n \zeta) &= \sum_{m=1,2,\dots} X_{mn1} \cos(\alpha_m \zeta) + X_{n1} \\ \sinh(u_n \zeta) &= \sum_{m=1,2,\dots} X_{mn2} \sin(\alpha_m \zeta), \quad \zeta \cosh(u_n \zeta) = \sum_{m=1,2,\dots} X_{mn3} \sin(\alpha_m \zeta) \\ \sinh(u_n \zeta) &= \sum_{m=1,2,\dots} X_{mn0}^* \sin(\beta_m \zeta), \quad \zeta \cosh(u_n \zeta) = \sum_{m=1,2,\dots} X_{mn1}^* \sin(\beta_m \zeta) \\ \cosh(u_n \zeta) &= \sum_{m=1,2,\dots} X_{mn2}^* \cos(\beta_m \zeta), \quad \zeta \sinh(u_n \zeta) = \sum_{m=1,2,\dots} X_{mn3}^* \cos(\beta_m \zeta) \end{aligned} \tag{33}$$

where X_{n0} , X_{n1} , $X_{mn0} \sim X_{mn3}$, and $X_{mn0}^* \sim X_{mn3}^*$ are listed in Appendix.

Substituting Eq. (33) into Eqs. (28), (29), (31) and (32), the stresses can be expressed in the final form as

$$\begin{cases} \frac{\sigma_{r0}}{2G} h^2 = \omega_{m0} \cos(\alpha_m \zeta) + \sum_{n=1,2,\dots}^{\infty} eX_{mn0} \cos(\alpha_n \zeta) + eX_m \\ \frac{\tau_{rz0}}{2G} h^2 = \omega_{m1} \sin(\alpha_m \zeta) + \sum_{n=1,2,\dots}^{\infty} eX_{mn1} \sin(\alpha_n \zeta) \\ \frac{\sigma_{r1}}{2G} h^2 = \lambda_{m0} \cos(\alpha_m \zeta) + \sum_{n=1,2,\dots}^{\infty} fX_{mn0} \cos(\alpha_n \zeta) + fX_m \\ \frac{\tau_{rz1}}{2G} h^2 = \lambda_{m1} \sin(\alpha_m \zeta) + \sum_{n=1,2,\dots}^{\infty} fX_{mn1} \sin(\alpha_n \zeta) \\ \frac{\sigma_{r0}^*}{2G} h^2 = \omega_{m0}^* \sin(\beta_m \zeta) + \sum_{n=1,2,\dots}^{\infty} eX_{mn0}^* \sin(\beta_n \zeta) \\ \frac{\tau_{rz0}^*}{2G} h^2 = \omega_{m1}^* \cos(\beta_m \zeta) + \sum_{n=1,2,\dots}^{\infty} eX_{mn1}^* \cos(\beta_n \zeta) \\ \frac{\sigma_{r1}^*}{2G} h^2 = \lambda_{m0}^* \sin(\beta_m \zeta) + \sum_{n=1,2,\dots}^{\infty} fX_{mn0}^* \sin(\beta_n \zeta) \\ \frac{\tau_{rz0}^*}{2G} h^2 = \lambda_{m1}^* \cos(\beta_m \zeta) + \sum_{n=1,2,\dots}^{\infty} fX_{mn1}^* \cos(\beta_n \zeta) \end{cases} \quad (34)$$

where eX_{mn0} , eX_{mn1} , eX_m , fX_{mn0} , fX_{mn1} , fX_m , eX_{mn0}^* , eX_{mn1}^* , fX_{mn0}^* , and fX_{mn1}^* are listed in Appendix.

3.4. Determination of the stress coefficients

By a linear combination of the stresses in Eqs. (30) and (34), the complete stress solution for the current problem can be written as

$$\begin{aligned} \sigma_r &= \sum_{m=1,2,\dots}^{\infty} (A_m \sigma_{r0} + B_m \sigma_{r1} + A_m^* \sigma_{r0}^* + B_m^* \sigma_{r1}^*) + A_0 \sigma_{r2} \\ \tau_{rz} &= \sum_{m=1,2,\dots}^{\infty} (A_m \tau_{rz0} + B_m \tau_{rz1} + A_m^* \tau_{rz0}^* + B_m^* \tau_{rz1}^*) \\ \sigma_{\theta} &= \sum_{m=1,2,\dots}^{\infty} (A_m \sigma_{\theta0} + B_m \sigma_{\theta1} + A_m^* \sigma_{\theta0}^* + B_m^* \sigma_{\theta1}^*) + A_0 \sigma_{\theta2} \end{aligned} \quad (35)$$

where A_0 , A_m , B_m , A_m^* , and B_m^* are the unknown coefficients of the stresses.

Since there are only axisymmetric radial residual stresses in the undrilled plate, the shear stress $\tau_{rz}(\rho_0, \zeta)$ is zero after the hole drilling. The radial stress $\sigma_{r0}(\zeta)$ can be expanded into the Fourier series as

$$\sigma_{r0}(\zeta) = E_0 + \sum_{m=1,2,\dots}^{\infty} E_m \cos(\alpha_m \zeta) + \sum_{m=1,2,\dots}^{\infty} E_m^* \sin(\beta_m \zeta) \quad (36)$$

where E_0 , E_m , and E_m^* are the coefficients of the Fourier expansion.

Hence, the stress boundary conditions on the hole are

$$\tau_{rz}(\rho_0, \zeta) = 0, \quad \sigma_r(\rho_0, \zeta) = \sigma_{r0}(\zeta) \quad (37)$$

Substituting Eqs. (35) and (36) into Eq. (37) and using the orthogonality of 1, $\cos(\alpha_m \zeta)$, and $\sin(\beta_m \zeta)$ on the interval $[-1, 1]$, it yields

$$\begin{aligned} A_0 + \sum_{m=1,2,\dots}^{Max-1} A_m eX_m + \sum_{m=1,2,\dots}^{Max-1} B_m fX_m &= E_0 \\ A_k \omega_{k0} + B_k \lambda_{k0} + \sum_{m=1,2,\dots}^{Max-1} A_m eX_{mk0} + \sum_{m=1,2,\dots}^{Max-1} B_m fX_{mk0} &= E_k \\ A_k \omega_{k1} + B_k \lambda_{k1} + \sum_{m=1,2,\dots}^{Max-1} A_m eX_{mk1} + \sum_{m=1,2,\dots}^{Max-1} B_m fX_{mk1} &= 0 \\ A_k^* \omega_{k0}^* + B_k^* \lambda_{k0}^* + \sum_{m=1,2,\dots}^{Max} A_m^* eX_{mk0}^* + \sum_{m=1,2,\dots}^{Max} B_m^* fX_{mk0}^* &= E_k^* \end{aligned} \quad (38)$$

$$A_k^* \omega_{k1}^* + B_k^* \lambda_{k1}^* + \sum_{m=1,2,\dots}^{Max} A_m^* eX_{mk1}^* + \sum_{m=1,2,\dots}^{Max} B_m^* fX_{mk1}^* = 0$$

where Max is the truncation value for m to ensure the convergence of the solution; $k = 1, 2, \dots, Max - 1$ for A_k, B_k, E_k and $k = 1, 2, \dots, Max$ for A_k^*, B_k^*, E_k^* .

The coefficients A_0, A_m, B_m, A_m^* , and B_m^* can be solved from Eq. (38). Then, the stresses in the plate can be calculated using Eq. (35). Since the normal stress σ_z on the surfaces $\zeta = \pm 1$ of the plate is zero, the surface radial strain $\epsilon_r(\rho, \pm 1)$ is calculated using Hooke's law as

$$\epsilon_r(\rho, \pm 1) = \frac{1}{2G(1 + \nu)} [\sigma_r(\rho, \pm 1) - \nu \sigma_{\theta}(\rho, \pm 1)] \quad (39)$$

4. The reverse procedure

It is assumed that the stresses are continuous and infinite differentiable at any point throughout the thickness. Therefore, the radial stress $\sigma_{r0}(\zeta)$ may be expanded by the Maclaurin series as

$$\sigma_{r0}(\zeta) = \sum_{n=0}^{\infty} L_n \zeta^n \quad (40)$$

where L_n is the undetermined coefficient.

It should be noted that the first few terms is generally enough to approach $\sigma_{r0}(\zeta)$ due to the convergence of series. The series is truncated to N in practice. The coefficient L_n can be determined based on the radial strains on the surfaces of the plate. The relationship between the radial stress and the surface radial strains is established in the form of matrix to conduct the reverse procedure. The constant vector \mathbf{E} ($= [E_0, E_1, \dots, E_{Max-1}, 0, \dots, 0, E_1^*, E_2^*, \dots, E_{Max}^*, 0, \dots, 0]^T$) can be calculated by the coefficient vector \mathbf{L} ($= [L_0, L_1, \dots, L_N]^T$) as

$$\mathbf{E} = \mathbf{M}_1 \mathbf{L} \quad (41)$$

where the matrix \mathbf{M}_1 is listed in Appendix.

According to Eq. (38), the relationship between the coefficient vector of the stresses \mathbf{C} ($= [A_0, A_1, \dots, A_{max-1}, B_1, \dots, B_{Max-1}, A_1^*, \dots, A_{Max}^*, B_1^*, \dots, B_{Max}^*]^T$) and \mathbf{E} is

$$\mathbf{C} = \mathbf{M}_2^{-1} \mathbf{E} \quad (42)$$

where the matrix \mathbf{M}_2 is listed in Appendix.

Substituting Eq. (35) into Eq. (39), the surface radial strain vector $\boldsymbol{\epsilon}$ ($= [\epsilon_r(\rho_{11}, 1), \epsilon_r(\rho_{12}, 1), \dots, \epsilon_r(\rho_{1N_1}, 1), \epsilon_r(\rho_{b1}, -1), \epsilon_r(\rho_{b2}, -1), \dots, \epsilon_r(\rho_{bN_2}, -1)]^T$) is calculated by \mathbf{C} as

$$\boldsymbol{\epsilon} = \mathbf{M}_3 \mathbf{C} \quad (43)$$

where N_1 and N_2 are the numbers of the measuring points at the top and bottom surfaces, respectively; ρ_{1i} and ρ_{bj} ($1 \leq i \leq N_1, 1 \leq j \leq N_2$) are the dimensionless radial distances of the i th and j th measuring points at the top and bottom surfaces, respectively; the matrix \mathbf{M}_3 is listed in Appendix.

From Eqs. (41)~(43), the relationship between \mathbf{L} and $\boldsymbol{\epsilon}$ are finally obtained as following

$$\boldsymbol{\epsilon} = \mathbf{M} \mathbf{L} \quad (44)$$

where the matrix \mathbf{M} is $\mathbf{M}_3 \mathbf{M}_2^{-1} \mathbf{M}_1$.

For convenience, the measured surface radial strain is denoted by $\boldsymbol{\epsilon}_m$ ($= [\epsilon_{m1}(\rho_{11}), \epsilon_{m1}(\rho_{12}), \dots, \epsilon_{m1}(\rho_{1N_1}), \epsilon_{mb}(\rho_{b1}), \epsilon_{mb}(\rho_{b2}), \dots, \epsilon_{mb}(\rho_{bN_2})]^T$). The following function is introduced to describe the difference between the predicted and measured surface radial strains

$$f(\mathbf{L}) = (\mathbf{M} \mathbf{L} - \boldsymbol{\epsilon}_m)^T (\mathbf{M} \mathbf{L} - \boldsymbol{\epsilon}_m) \quad (45)$$

The predicted surface radial strain should be as close to the measured surface radial strain as possible. In other words, $f(\mathbf{L})$ should take

the stationary value. Hence, by calculating the derivative of f with respect to \mathbf{L} , it yields

$$\frac{\partial f}{\partial \mathbf{L}} = 2\mathbf{M}^T(\mathbf{M}\mathbf{L} - \boldsymbol{\epsilon}_m) = \mathbf{0} \quad (46)$$

The coefficient vector \mathbf{L} can be solved by Eq. (46). Then, the measured through-thickness axisymmetric radial stress $\sigma_{r0m}(\zeta)$ can be calculated by Eq. (40). The coefficient of determination R^2 and root-mean-square deviation $RMSE$ are used to evaluate the prediction, which are defined by

$$R^2 = 1 - \frac{\int_{-1}^1 [\sigma_{r0}(\zeta) - \sigma_{r0m}(\zeta)]^2 d\zeta}{\int_{-1}^1 [\sigma_{r0}(\zeta) - \bar{\sigma}_{r0}]^2 d\zeta} \quad (47a)$$

$$RMSE = \sqrt{\frac{\int_{-1}^1 [\sigma_{r0}(\zeta) - \sigma_{r0m}(\zeta)]^2 d\zeta}{2}} \quad (47b)$$

where $\bar{\sigma}_{r0}$ is the average value of $\sigma_{r0}(\zeta)$ on the interval $[-1, 1]$. It should be noted the prediction is close to the real one when R^2 approaches to 1 and $RMSE$ is small.

5. Validation

It is well known that FEM can accurately simulate the elastic behaviors of materials. Fig. 2 illustrates the comparison of the top surface radial strain by the present model with that by FEM. In the figure, the distribution of the through-thickness axisymmetric radial stress is plotted on the subfigure. Four different distributions of the through-thickness axisymmetric radial stress were considered to validate the proposed model. The FEM results were obtained by the numerical program ABAQUS as shown in Fig. 3. A linear elastic material was assigned to the plate with Young's modulus 210 GPa and Poisson's ratio 0.3. The plate was simulated using eight-node 3-D solid elements with reduced integration (C3D8R). The thickness of the plate was 0.1 m. The radius of the hole was 0.1 m and the radius of the plate was set to ten times the radius of the hole to reduce the influence of the boundary. The element size at the hole edge was 0.01 m and increased from 0.01 m at the hole edge to 0.04 m at the plate edge. The element size was 0.01 m along the plate thickness. The FEM model was partitioned in the thickness and the axisymmetric radial stress was applied on the partitioned segments of the hole by creating the analytical field in the thickness.

From Fig. 2, it can be seen that the present solutions agree well with those by FEM, indicating the good accuracy of the present model. The slight difference between the two methods in Fig. 2(d) may originate from the mesh and boundary conditions in FEM. From Fig. 2(a), it can be observed that the results obtained by the present model, FEM, and plane stress solution are very close. This indicates that the uniform stress distribution can be evaluated based on the plane stress solution. From Fig. 2(b), it can be found that the linear stress distributions have negligible influence on the surface radial strain when the radial stresses at $\zeta = 1$ are the same. This indicates that for the linear stress distribution, the radial strain on the top surface (bottom surface) is mainly affected by the radial stress at $\zeta = 1$ ($\zeta = -1$). Inversely, the linear distribution may be determined by measuring the surface radial strains at the top and bottom surfaces simultaneously. Moreover, it is observed that the radial strain decreases rapidly first and then slowly. At distances that are three times the radius of the hole away, the strain is less more than 15% of that at the hole edge.

Fig. 4 shows the comparison between the predicted and real distributions, in which the surface radial strains for the reverse procedure are retrieved from the post-processing of FEM, as shown in Table 1. It can be found that the prediction and real distribution are in good agreement, indicating the good accuracy for the reverse procedure. The maximum deviation occurs in the parabolic distribution, which may be caused by the mesh and boundary conditions set in FEM and the limited series terms.

Table 1

The surface radial strain values calculated by FEM.

ρ	Linear		Bi-linear		Parabolic	
	ϵ_{mt} [$\mu\epsilon$]	ϵ_{mb} [$\mu\epsilon$]	ϵ_{mt} [$\mu\epsilon$]	ϵ_{mb} [$\mu\epsilon$]	ϵ_{mt} [$\mu\epsilon$]	ϵ_{mb} [$\mu\epsilon$]
1.20	29.7	13.4	20.5	4.3	14.7	14.7
1.42	21.2	9.5	14.7	3.0	10.1	10.1
1.66	15.6	7.0	10.8	2.1	6.9	6.9
1.78	13.4	6.0	9.3	1.7	5.7	5.7
1.91	11.7	5.2	8.0	1.4	4.7	4.7
2.18	8.9	4.0	6.1	1.0	3.3	3.3

6. Parametric study

For convenience, the following typical parameters will be adopted in the subsequent analysis, including the dimensionless radius of the hole $\rho_0 = 1$, Young's modulus of the plate $E_p = 210$ GPa, and Poisson's ratio $\nu = 0.3$. Since the matrix $\mathbf{M}^T\mathbf{M}$ determines the coefficient vector \mathbf{L} according to Eq. (46), the condition number of this matrix should not be very large to ensure the stability of the solution. Fig. 5 gives the relationship between the condition number of $\mathbf{M}^T\mathbf{M}$ based on the L_2 norm and the measuring points spacing $\Delta\rho$, where the measuring points closest to the center are located at 1.2 times the radius. The condition number declines with the increase of the number of the measuring points. This is understood based on the fact that higher measuring redundancy leads to more accurate measurement. The condition number rises with the increase of N or the decrease of the spacing of the measuring points $\Delta\rho$. Therefore, a more stable measurement can be achieved by choosing small N value and large $\Delta\rho$. Conversely, the matrix $\mathbf{M}^T\mathbf{M}$ may be ill-conditioned for a very large N value or in case of a small number of measuring points, leading to enormous errors in the prediction. In the following analysis, the radial strains for both the top and bottom surfaces are located at distances that are 1.2, 1.4, 1.6, 1.8, 2, 2.2 times the radius away from the center of the hole, as shown in Fig. 6.

6.1. Influence of the series term

Fig. 7 shows the contribution of the individual term of the series in Eq. (40) to the surface radial strain, in which the values for all terms at $\zeta = 1$ are 10 MPa. The surface radial strain decreases with the increase of the order of the even or odd terms. This can be explained by that the interior radial stress approaches to zero for a high order term. In addition, the surface radial strain calculated by the adjacent even and odd terms (e.g., the zeroth and first terms) are close to each other. However, this is not the case for the bottom surface due to the opposite distributions in the lower half of the plate. Hence, the adjacent terms may be determined by measuring the top and bottom surface radial strains simultaneously. Moreover, the surface radial strain values are close to each other and approach zero when $\rho > 3$, implying that the measurements beyond 3 times the radius of the hole have little sense.

6.2. Prediction of the residual stress by peening

In general, measurement errors include random errors and systematic errors. For DIC, the random errors are mainly caused by the image noise while the systematic errors are mainly due to algorithms, which can be reduced by improving the procedure, e.g. iDIC. To test the sensitivity of the proposed mode to noise, the Gaussian noise with zero mean value and varied standard deviations is added to the real surface radial strains for the prediction of the residual stresses by peening. Fig. 8 presents the predictions of the residual stress by peening, in which the thickness is normalized to 2. There are in good agreement with high R^2 and low $RMSE$ even for the noise of a standard deviation of 5% relative to the real strain values. The deviation increases with the increase of the standard deviation. The maximum distinction occurs at the turn of the distribution, which may be explained by the high standard deviation and the limited terms of the series.

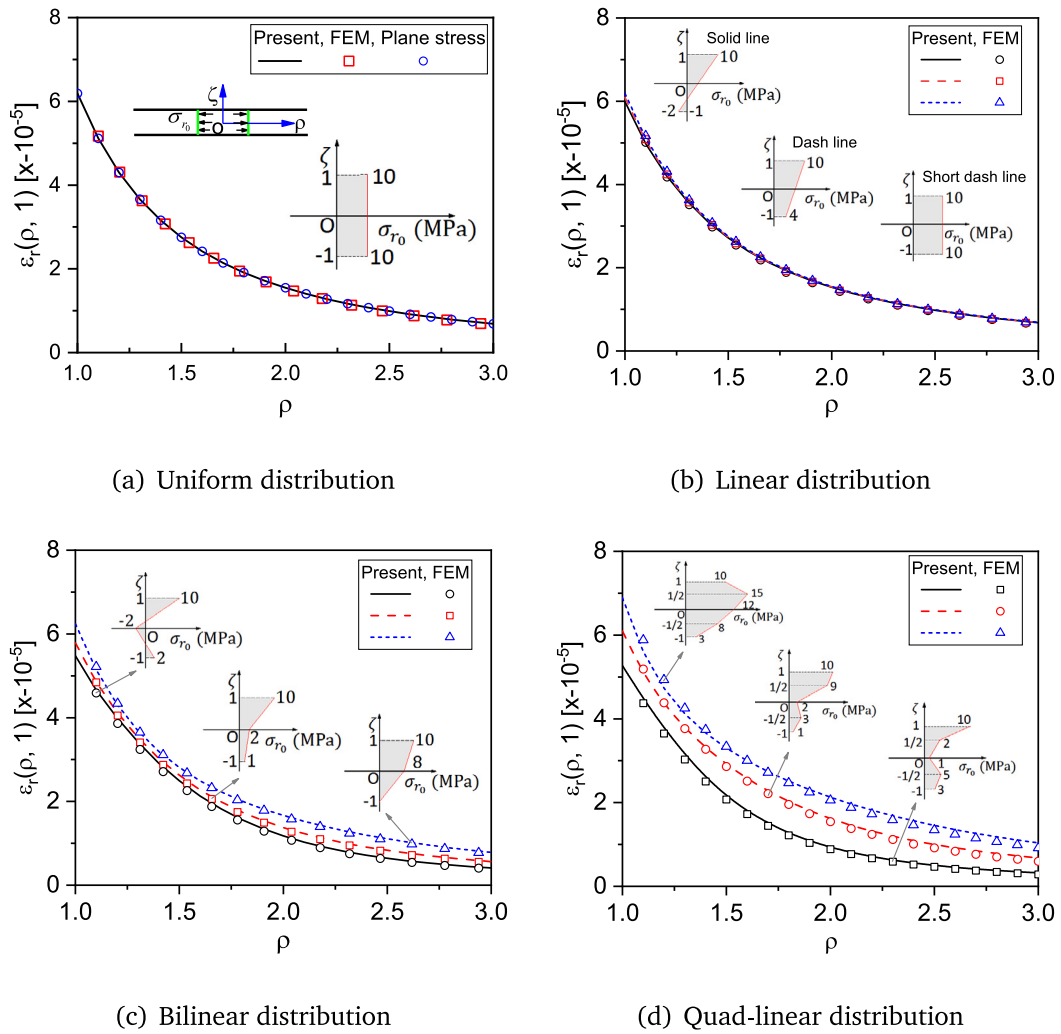


Fig. 2. Validation of the present model with FEM.

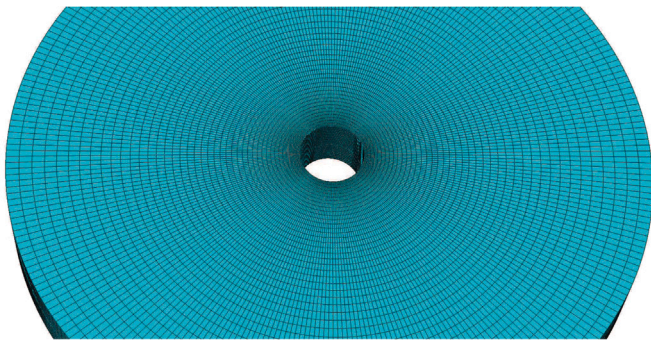


Fig. 3. The FEM model.

6.3. Prediction of the axisymmetric radial stress

In this section, the error obeying normal distribution with a standard deviation of 2.5% (relative to the real strain values) is added to the surface radial strains to represent the noise. To avoid being confused with the true measured values, the strain values adding the error are denoted by the simulated values as shown in the subgraph. Fig. 9 shows the prediction of the axisymmetric radial stress in the linear distribution. The predictions are very close to the real distributions. It

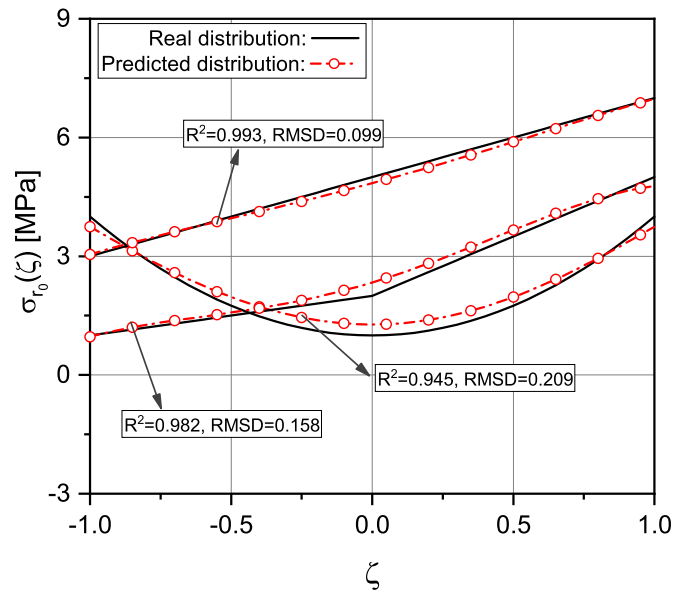


Fig. 4. The predicted distributions ($N = 4$).

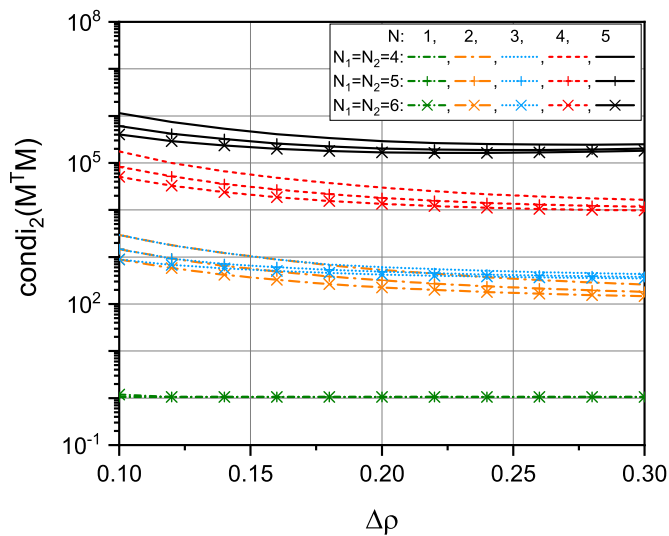


Fig. 5. The relationship between the condition number of $M^T M$ and $\Delta\rho$.

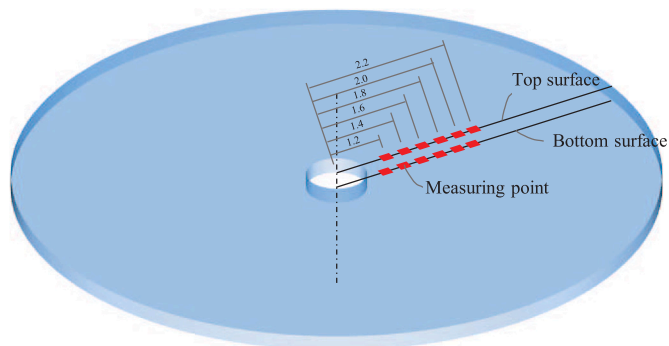


Fig. 6. The arrangement of the measuring points.

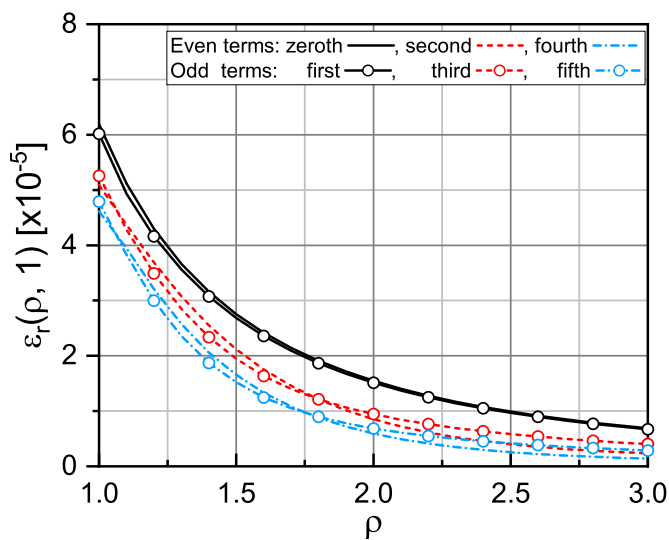


Fig. 7. The influence of the individual term of the series on the surface radial strain.

can be seen that the prediction by setting $N = 1$ is pretty accurate. This is because $N = 1$ corresponds to a linear distribution.

Fig. 10 shows the prediction of the axisymmetric radial stress in the bi-linear distribution. The first four terms ($N = 3$) of the series cannot present the real distribution properly. Although there is a high

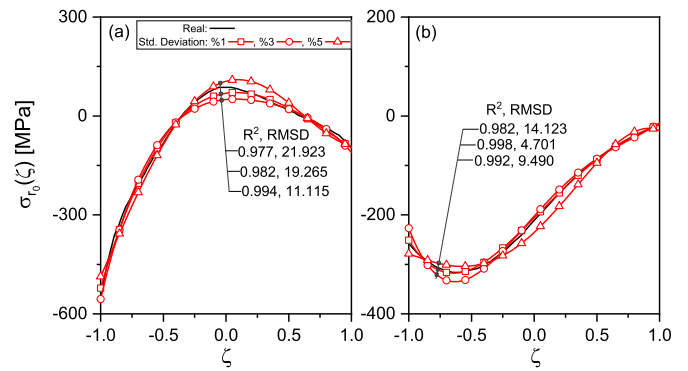


Fig. 8. The predictions of the residual stress by peening ($N = 4$): (a) hammer peened 5 times (initially free-stress samples) [30]; (b) shot peening intensity 0.26 mm A for C-1020 material cold rolled [31].

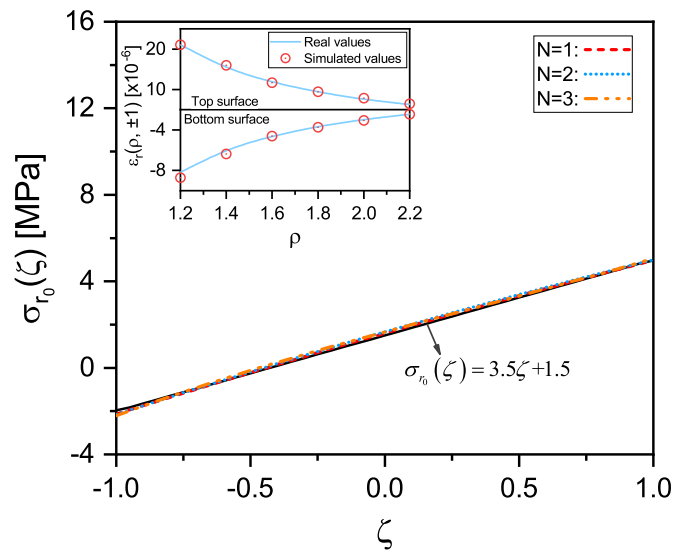


Fig. 9. Prediction of the axisymmetric radial stress in the linear distribution.

derivation on the center between the predicted and real distributions, it can give a similar trend using $N = 3$. The deviation may come from the representation of the radial stress using the limited terms of the series. Nevertheless, the first five or six terms ($N = 4$ or $N = 5$) can be suitable to predict the bi-linear distribution of the stress, e.g., tension at the surfaces but compression at the center of the plate.

As for a more complex polygonal distribution, Fig. 11 shows the prediction of the axisymmetric radial stress in the quad-linear distribution. It can be seen that the first four terms ($N = 3$) of the series cannot give a satisfying prediction of the stress although it presents the variation trend of the stress along the thickness. The main reason may be due to the fact that the derivative of the stress is not continuous at the tip and the stress cannot be expressed by Eq. (42) properly when $N \leq 3$. However, it can give a reasonable overall prediction by setting $N \geq 4$ and a better result for $N = 5$. Thus, the terms with orders larger than 3 have significant effects on the stress distribution. This can be understood because for the rapid variation of the stress along the thickness, the high order terms are important to constitute the stress. Therefore, more terms of the series can give more accurate evaluations. To conclude, the first six terms ($N = 5$) can be adopted to evaluate the quad-linear distribution of the stress.

Fig. 12 illustrates the prediction of the axisymmetric radial stress in the sinusoidal distribution. It can be found that the predictions calculated by $N = 3$ and $N = 4$ are both close to the real distribution.

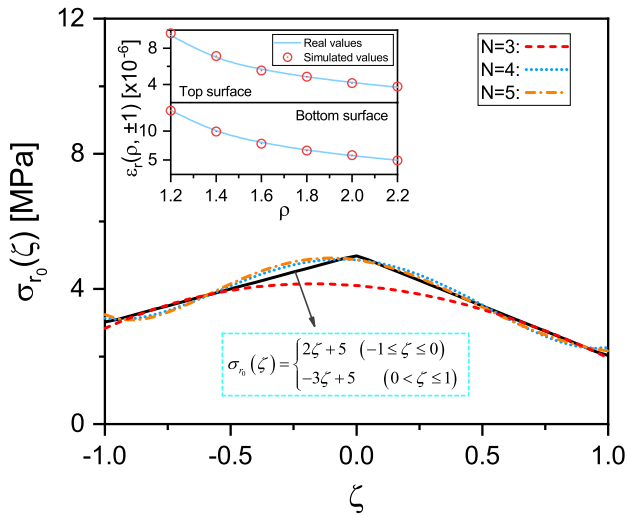


Fig. 10. Prediction of the axisymmetric radial stress in the bi-linear distribution.

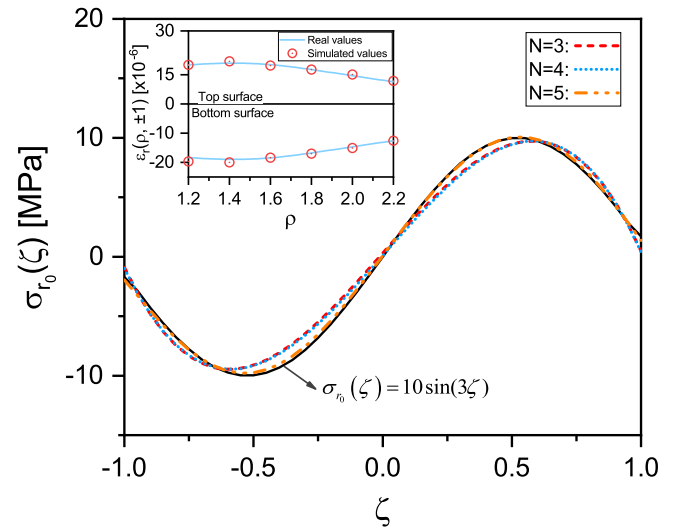


Fig. 12. Prediction of the axisymmetric radial stress in the sinusoidal distribution.

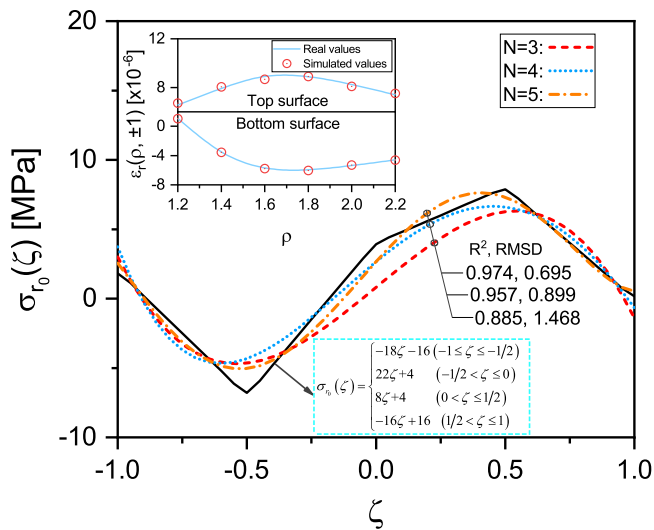


Fig. 11. Prediction of the axisymmetric radial stress in the quad-linear distribution.

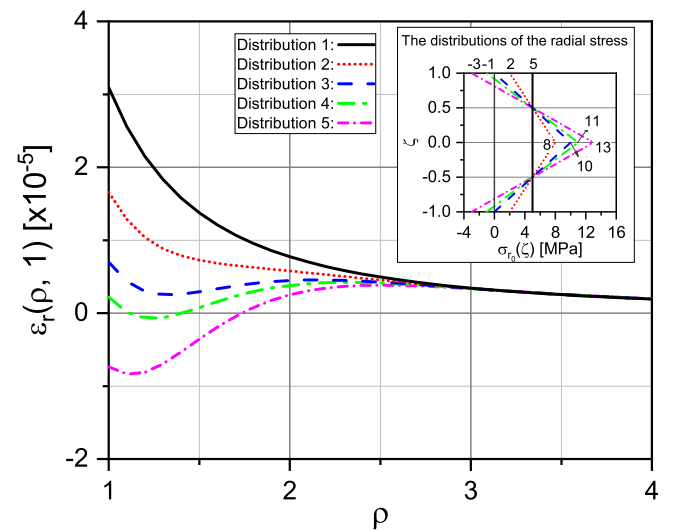


Fig. 13. The influences of the stress distributions with the same resultant forces on the surface radial strain.

Moreover, A satisfactory match between the prediction and the real distribution can be achieved when $N = 5$.

6.4. Analysis of the resultant force and moment per unit hole circumference

The total effect of the through-thickness axisymmetric radial stress may be treated as the resultant force and the moment per unit hole circumference acting at the center of the hole, which are defined by

$$Force = \int_{-1}^1 h\sigma_{r_0}(\zeta)d\zeta \tag{48}$$

$$Moment = \int_{-1}^1 h^2\zeta\sigma_{r_0}(\zeta)d\zeta$$

The force and moment can be used to evaluate the deformation of the plate according to the theory of plate. Figs. 13 and 14 show the influences of the stress distributions with the same forces and moments on the surface radial strain, respectively. In Fig. 13, the moments are zero and the forces are the same for the five different stress distributions. It can be seen that the stress distributions affect the strain within 2.7 times the radius of the hole. In Fig. 14, the forces are zero and moments are the same for the three different stress distributions.

Similar to Fig. 13, the stress distributions have great influences on the strain within 2.5 the times the radius of the hole. From Figs. 13 and 14, it may be concluded that in order to measure the resultant force and moment, the surface radial strains beyond 2.7 times the hole radius need to be measured to eliminate the influence of the stress distribution.

Since the strain beyond 2.7 times the hole radius is slightly affected by the stress distribution, the stress along the thickness is assumed to be linear distribution so as to conveniently evaluate the resultant force and moment. Referring to Fig. 2(b), the surface radial strain can be determined by the stress at the corresponding edge of the hole according to the plane stress solution. Therefore, the stress in linear distribution can be measured by the hole-drilling strain gauge method, provided that the top and bottom surface radial strains beyond 2.7 times the hole radius are measured simultaneously.

7. Further discussion

Residual stresses play an important role in the stiffness, stability, fracture, and fatigue of the component. Although the hole-drilling

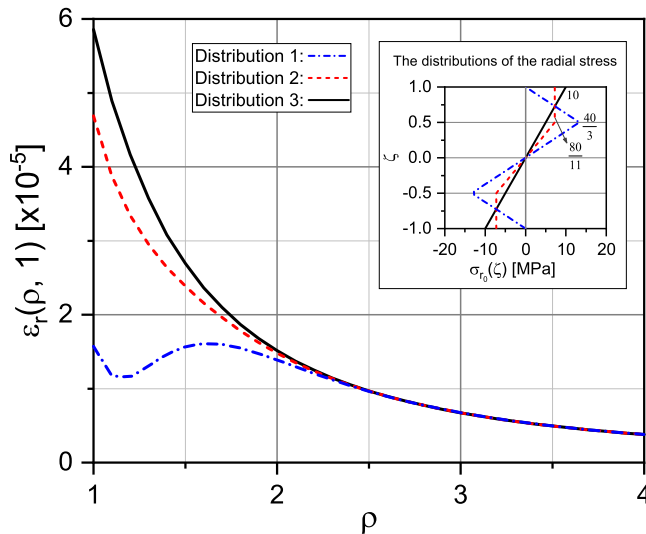


Fig. 14. The influences of the stress distributions with the same moments on the surface radial strain.

strain gauge method has been commonly implemented, it may not be able to measure the stresses along the whole thickness of the plate. This paper proposes an analytical model to measure the through-thickness axisymmetric radial residual stress with hole drilling. It should be noted that the general in-plane principal residual stresses $\sigma_1(z)$ and $\sigma_2(z)$ varying along the thickness can be expressed by $\sigma_r(z)$ and $\tau_{r\theta}(z)$ in the cylinder coordinate system as

$$\begin{aligned} \sigma_r(\theta, z) &= \frac{\sigma_1(z) + \sigma_2(z)}{2} + \frac{\sigma_1(z) - \sigma_2(z)}{2} \cos(2\theta) \\ \tau_{r\theta}(\theta, z) &= \frac{\sigma_1(z) - \sigma_2(z)}{2} \sin(2\theta) \end{aligned} \quad (49)$$

If the residual stresses are isotropic (equi-biaxial), i.e., $\sigma_1(z) = \sigma_2(z)$, there is only axisymmetric radial residual stress released after the hole drilling. Therefore, the through-thickness isotropic residual stress can be measured according to the proposed model. The measurement of the terms relevant to 2θ needs to be further studied to establish a general model for the measurement of the in-plane through-thickness residual stresses. Besides, the experimental research adopting the developed model will also be carried out in the future to investigate the influence of the residual stresses on the mechanical properties of the component.

8. Conclusion

The analytical solution for the strain of a plate with a hole subjected to the through-thickness axisymmetric radial stress is obtained based on the three-dimensional elastic theory. It is assumed that the through-thickness axisymmetric radial residual stress can be expanded into the Maclaurin series. Then, the reverse procedure is proposed to determine the coefficients of the series by minimizing the predicted and measured surface radial strains with hole drilling. The model is validated by FEM for a few typical distribution types of the axisymmetric radial stress along the thickness. From the study, some major conclusions can be drawn as follows

- (1) More stable results can be achieved by choosing fewer terms of the Maclaurin series and more measuring points with large spacing. The surface radial strain decreases with the increase of the order of the even or odd terms.
- (2) The residual stress caused by peening can be predicted with the proposed model. The first two terms of the Maclaurin series can be used to predict linear distributions while five terms are required for more satisfactory predictions of bi-linear, quad-linear, and sinusoidal distributions.

- (3) The stress distributions with the same resultant forces or moments per unit hole circumference mainly affect the surface radial strain within 2.7 times the hole radius. The force and moment can be measured by the hole-drilling strain gauge method, provided that the top and bottom surface radial strains beyond 2.7 times hole radius are measured simultaneously.

CRedit authorship contribution statement

Huan Liu: Formal analysis, Methodology, Software, Writing – original draft. **Lu Deng:** Conceptualization, Supervision. **YuLong He:** Writing – review & editing.

Declaration of competing interest

The authors declare that they have no known competing financial interests or personal relationships that could have appeared to influence the work reported in this paper.

Acknowledgments

The study was supported by the Science and Technology Innovation Plan Project of Hunan Province, China (Grant 2018NK2053) and Changsha Excellent Innovative Youth Training Program, China (Project No. kq1802001).

Appendix

The coefficients $\omega_{m0} \sim \omega_{m2}$ and $e_{mn0} \sim e_{mn5}$ in Eq. (28) are

$$\begin{aligned} \omega_{m0} &= \alpha_m^2 K_0(\alpha_m \rho) + \frac{\alpha_m K_1(\alpha_m \rho)}{\rho} \\ e_{mn0} &= -u_n^2 (c_{mn0} + 3c_{mn1}) P_0(u_n \rho) + u_n (c_{mn0} + \eta c_{mn1}) \frac{P_1(u_n \rho)}{\rho} \\ e_{mn1} &= 2u_n^2 c_{mn1} \left[-u_n P_0(u_n \rho) + \frac{P_1(u_n \rho)}{\rho} \right], \quad \omega_{m1} = \alpha_m^2 K_1(\alpha_m \rho) \\ e_{mn2} &= -u_n^2 (c_{mn0} + c_{mn1}) P_1(u_n \rho), \quad e_{mn3} = -2u_n^3 c_{mn1} P_1(u_n \rho) \\ \omega_{m2} &= -\frac{\alpha_m K_1(\alpha_m \rho)}{\rho}, \quad e_{mn5} = -2u_n^2 c_{mn1} \frac{P_1(u_n \rho)}{\rho} \\ e_{mn4} &= u_n^2 (\eta - 3) c_{mn1} P_0(u_n \rho) - u_n (c_{mn0} + \eta c_{mn1}) \frac{P_1(u_n \rho)}{\rho} \end{aligned} \quad (A.1)$$

The coefficients $\lambda_{m0} \sim \lambda_{m2}$ and $f_{mn0} \sim f_{mn5}$ in Eq. (29) are

$$\begin{aligned} \lambda_{m0} &= 6\alpha_m^2 K_0(\alpha_m \rho) + 2\alpha_m^3 \rho K_1(\alpha_m \rho) + (\eta + 5) \alpha_m \frac{K_1(\alpha_m \rho)}{\rho} \\ f_{mn0} &= -u_n^2 (d_{mn0} + 3d_{mn1}) P_0(u_n \rho) + u_n (d_{mn0} + \eta d_{mn1}) \frac{P_1(u_n \rho)}{\rho} \\ f_{mn1} &= 2u_n^2 d_{mn1} \left[-u_n P_0(u_n \rho) + \frac{P_1(u_n \rho)}{\rho} \right], \quad f_{mn3} = -2u_n^3 d_{mn1} P_1(u_n \rho) \\ \lambda_{m1} &= 2\alpha_m^3 \rho K_0(\alpha_m \rho) + 4\alpha_m^2 K_1(\alpha_m \rho) \\ f_{mn2} &= -u_n^2 (d_{mn0} + d_{mn1}) P_1(u_n \rho), \quad f_{mn5} = -2u_n^2 d_{mn1} \frac{P_1(u_n \rho)}{\rho} \\ \lambda_{m2} &= (1 - \eta) \alpha_m^2 K_0(\alpha_m \rho) - (\eta + 5) \frac{\alpha_m K_1(\alpha_m \rho)}{\rho} \\ f_{mn4} &= u_n^2 (\eta - 3) d_{mn1} P_0(u_n \rho) - u_n (d_{mn0} + \eta d_{mn1}) \frac{P_1(u_n \rho)}{\rho} \end{aligned} \quad (A.2)$$

The coefficients $X_{n0}, X_{n1}, X_{mn0} \sim X_{mn3}$, and $X_{mn0}^* \sim X_{mn3}^*$ in Eq. (33) are

$$\begin{aligned} X_{n0} &= \frac{\sinh u_n}{u_n}, \quad X_{n1} = \frac{\cosh u_n}{u_n} - \frac{\sinh u_n}{u_n^2} \\ X_{mn0} &= \frac{2(-1)^m u_n \sinh u_n}{u_n^2 + \alpha_m^2}, \\ X_{mn1} &= 2(-1)^m \left[\frac{u_n \cosh u_n}{u_n^2 + \alpha_m^2} - \frac{(u_n^2 - \alpha_m^2) \sinh u_n}{(u_n^2 + \alpha_m^2)^2} \right] \end{aligned}$$

$$\begin{aligned}
 X_{mn2} &= 2(-1)^{m+1} \frac{\alpha_m \sinh(u_n)}{u_n^2 + \alpha_m^2}, \\
 X_{mn3} &= 2(-1)^{m+1} \alpha_m \left[\frac{\cosh u_n}{u_n^2 + \alpha_m^2} - \frac{2u_n \sinh u_n}{(u_n^2 + \alpha_m^2)^2} \right] \\
 X_{mn0}^* &= \frac{2(-1)^{m+1} u_n \cosh u_n}{u_n^2 + \beta_m^2}, \\
 X_{mn1}^* &= \frac{2(-1)^{m+1}}{u_n^2 + \beta_m^2} \left[u_n \sinh u_n - \frac{(u_n^2 - \beta_m^2) \cosh u_n}{u_n^2 + \beta_m^2} \right] \\
 X_{mn2}^* &= 2(-1)^{m+1} \frac{\beta_m \cosh(u_n)}{u_n^2 + \beta_m^2}, \\
 X_{mn3}^* &= \frac{2(-1)^{m+1} \beta_m}{u_n^2 + \beta_m^2} \left[\sinh u_n - \frac{2u_n \cosh u_n}{u_n^2 + \beta_m^2} \right]
 \end{aligned} \tag{A.3}$$

The coefficients eX_{mn0} , eX_{mn1} , eX_m , fX_{mn0} , fX_{mn1} , fX_m , eX_{mn0}^* , eX_{mn1}^* , fX_{mn0}^* , and fX_{mn1}^* in Eq. (34) are

$$\begin{aligned}
 eX_{mn0} &= \sum_{t=0,1,2,\dots}^{\infty} (e_{mt0} X_{nt0} + e_{mt1} X_{nt1}), \\
 eX_m &= \sum_{t=0,1,2,\dots}^{\infty} (e_{mt0} X_{t0} + e_{mt1} X_{t1}) \\
 eX_{mn1} &= \sum_{t=0,1,2,\dots}^{\infty} (e_{mt2} X_{nt2} + e_{mt3} X_{nt3}), \\
 fX_{mn0} &= \sum_{t=0,1,2,\dots}^{\infty} (f_{mt0} X_{nt0} + f_{mt1} X_{nt1}) \\
 fX_m &= \sum_{t=0,1,2,\dots}^{\infty} (f_{mt0} X_{t0} + f_{mt1} X_{t1}), \\
 fX_{mn1} &= \sum_{t=0,1,2,\dots}^{\infty} (f_{mt2} X_{nt2} + f_{mt3} X_{nt3}) \\
 eX_{mn0}^* &= \sum_{t=0,1,2,\dots}^{\infty} (e_{mt0}^* X_{nt0}^* + e_{mt1}^* X_{nt1}^*), \\
 eX_{mn1}^* &= \sum_{t=0,1,2,\dots}^{\infty} (e_{mt2}^* X_{nt2}^* + e_{mt3}^* X_{nt3}^*) \\
 fX_{mn0}^* &= \sum_{t=0,1,2,\dots}^{\infty} (f_{mt0}^* X_{nt0}^* + f_{mt1}^* X_{nt1}^*), \\
 fX_{mn1}^* &= \sum_{t=0,1,2,\dots}^{\infty} (f_{mt2}^* X_{nt2}^* + f_{mt3}^* X_{nt3}^*)
 \end{aligned} \tag{A.4}$$

The matrix M_1 in Eq. (41) is

$$M_1 = \begin{bmatrix} \frac{1}{2} \int_{-1}^1 1 d\zeta & \frac{1}{2} \int_{-1}^1 \zeta d\zeta & \dots & \frac{1}{2} \int_{-1}^1 \zeta^N d\zeta \\ \int_{-1}^1 \cos(\alpha_1 \zeta) d\zeta & \int_{-1}^1 \zeta \cos(\alpha_1 \zeta) d\zeta & \dots & \int_{-1}^1 \zeta^N \cos(\alpha_1 \zeta) d\zeta \\ \vdots & \vdots & \ddots & \vdots \\ \int_{-1}^1 \cos(\alpha_{Max-1} \zeta) d\zeta & \int_{-1}^1 \zeta \cos(\alpha_{Max-1} \zeta) d\zeta & \dots & \int_{-1}^1 \zeta^N \cos(\alpha_{Max-1} \zeta) d\zeta \\ \mathbf{0}_1 & \mathbf{0}_1 & \dots & \mathbf{0}_1 \\ \int_{-1}^1 \sin(\beta_1 \zeta) d\zeta & \int_{-1}^1 \zeta \sin(\beta_1 \zeta) d\zeta & \dots & \int_{-1}^1 \zeta^N \sin(\beta_1 \zeta) d\zeta \\ \vdots & \vdots & \ddots & \vdots \\ \int_{-1}^1 \sin(\beta_{Max} \zeta) d\zeta & \int_{-1}^1 \zeta \sin(\beta_{Max} \zeta) d\zeta & \dots & \int_{-1}^1 \zeta^N \sin(\beta_{Max} \zeta) d\zeta \\ \mathbf{0}_2 & \mathbf{0}_2 & \dots & \mathbf{0}_2 \end{bmatrix} \tag{A.5}$$

where $\mathbf{0}_1$ and $\mathbf{0}_2$ are the zero column vectors with $Max - 1$ and Max elements, respectively.

The matrix M_2 in Eq. (42) is

$$M_2 = \begin{bmatrix} 1 & \mathbf{eX} & \mathbf{fX} & \mathbf{0} & \mathbf{0} \\ \mathbf{0} & M_{1A} & M_{1B} & \mathbf{0} & \mathbf{0} \\ \mathbf{0} & M_{2A} & M_{2B} & \mathbf{0} & \mathbf{0} \\ \mathbf{0} & \mathbf{0} & \mathbf{0} & M_{1A}^* & M_{1B}^* \\ \mathbf{0} & \mathbf{0} & \mathbf{0} & M_{2A}^* & M_{2B}^* \end{bmatrix} \tag{A.6}$$

where $\mathbf{eX} = [eX_1, eX_2, \dots, eX_{Max-1}]$ and $\mathbf{fX} = [fX_1, fX_2, \dots, fX_{Max-1}]$; the sub-matrices M_{1A} , M_{1B} , M_{2A} , M_{2B} , M_{1A}^* , M_{1B}^* , M_{2A}^* , M_{2B}^* are

$$\begin{aligned}
 M_{1A} &= \begin{bmatrix} \omega_{10} + eX_{110} & eX_{210} & \dots & eX_{Max-110} \\ eX_{120} & \omega_{20} + eX_{220} & \dots & eX_{Max-120} \\ \vdots & \vdots & \ddots & \vdots \\ eX_{1Max-10} & eX_{2Max-10} & \dots & \omega_{Max-10} + eX_{Max-1Max-10} \end{bmatrix} \\
 M_{1B} &= \begin{bmatrix} \lambda_{10} + fX_{110} & fX_{210} & \dots & fX_{Max-110} \\ fX_{120} & \lambda_{20} + fX_{220} & \dots & fX_{Max-120} \\ \vdots & \vdots & \ddots & \vdots \\ fX_{1Max-10} & fX_{2Max-10} & \dots & \lambda_{Max-10} + fX_{Max-1Max-10} \end{bmatrix} \\
 M_{2A} &= \begin{bmatrix} \omega_{11} + eX_{111} & eX_{211} & \dots & eX_{Max-111} \\ eX_{121} & \omega_{21} + eX_{221} & \dots & eX_{Max-121} \\ \vdots & \vdots & \ddots & \vdots \\ eX_{1Max-11} & eX_{2Max-11} & \dots & \omega_{Max-11} + eX_{Max-1Max-11} \end{bmatrix} \\
 M_{2B} &= \begin{bmatrix} \lambda_{11} + fX_{111} & f_{211} & \dots & fX_{Max-111} \\ fX_{121} & \lambda_{21} + fX_{221} & \dots & fX_{Max-121} \\ \vdots & \vdots & \ddots & \vdots \\ fX_{1Max-11} & fX_{2Max-11} & \dots & \lambda_{Max-11} + fX_{Max-1Max-11} \end{bmatrix} \\
 M_{1A}^* &= \begin{bmatrix} \omega_{10}^* + eX_{110}^* & eX_{210}^* & \dots & eX_{Max10}^* \\ eX_{120}^* & \omega_{20}^* + eX_{220}^* & \dots & eX_{Max20}^* \\ \vdots & \vdots & \ddots & \vdots \\ eX_{1Max0}^* & eX_{2Max0}^* & \dots & \omega_{Max0}^* + eX_{MaxMax0}^* \end{bmatrix} \\
 M_{1B}^* &= \begin{bmatrix} \lambda_{10}^* + fX_{110}^* & fX_{210}^* & \dots & fX_{Max10}^* \\ fX_{120}^* & \lambda_{20}^* + fX_{220}^* & \dots & fX_{Max20}^* \\ \vdots & \vdots & \ddots & \vdots \\ fX_{1Max0}^* & fX_{2Max0}^* & \dots & \lambda_{Max0}^* + fX_{MaxMax0}^* \end{bmatrix} \\
 M_{2A}^* &= \begin{bmatrix} \omega_{11}^* + eX_{111}^* & eX_{211}^* & \dots & eX_{Max11}^* \\ eX_{121}^* & \omega_{21}^* + eX_{221}^* & \dots & eX_{Max21}^* \\ \vdots & \vdots & \ddots & \vdots \\ eX_{1Max1}^* & eX_{2Max1}^* & \dots & \omega_{Max1}^* + eX_{MaxMax1}^* \end{bmatrix} \\
 M_{2B}^* &= \begin{bmatrix} \lambda_{11}^* + fX_{111}^* & f_{211}^* & \dots & fX_{Max11}^* \\ fX_{121}^* & \lambda_{21}^* + fX_{221}^* & \dots & fX_{Max21}^* \\ \vdots & \vdots & \ddots & \vdots \\ fX_{1Max1}^* & fX_{2Max1}^* & \dots & \lambda_{Max1}^* + fX_{MaxMax1}^* \end{bmatrix}
 \end{aligned}$$

The matrix M_3 in Eq. (43) is

$$M_3 = \frac{1}{2G(1 + \nu)} \begin{bmatrix} M_{t1} & \mathbf{MA}_{t1} & \mathbf{MB}_{t1} & \mathbf{MA}_{t1}^* & \mathbf{MB}_{t1}^* \\ M_{t2} & \mathbf{MA}_{t2} & \mathbf{MB}_{t2} & \mathbf{MA}_{t2}^* & \mathbf{MB}_{t2}^* \\ \vdots & \vdots & \vdots & \vdots & \vdots \\ M_{tN_1} & \mathbf{MA}_{tN_1} & \mathbf{MB}_{tN_1} & \mathbf{MA}_{tN_1}^* & \mathbf{MB}_{tN_1}^* \\ M_{b1} & \mathbf{MA}_{b1} & \mathbf{MB}_{b1} & \mathbf{MA}_{b1}^* & \mathbf{MB}_{b1}^* \\ M_{b2} & \mathbf{MA}_{b2} & \mathbf{MB}_{b2} & \mathbf{MA}_{b2}^* & \mathbf{MB}_{b2}^* \\ \vdots & \vdots & \vdots & \vdots & \vdots \\ M_{bN_2} & \mathbf{MA}_{bN_2} & \mathbf{MB}_{bN_2} & \mathbf{MA}_{bN_2}^* & \mathbf{MB}_{bN_2}^* \end{bmatrix} \tag{A.7}$$

where M_{ti} , \mathbf{MA}_{ti} , \mathbf{MB}_{ti} , \mathbf{MA}_{ti}^* , \mathbf{MB}_{ti}^* , \mathbf{MA}_{bj} , \mathbf{MB}_{bj} , \mathbf{MA}_{bj}^* , \mathbf{MB}_{bj}^* ($1 \leq i \leq N_1$, $1 \leq j \leq N_2$) are as follows

$$\begin{aligned}
 M_{ti} &= \sigma_{r2}(\rho_{ti}) - \nu \sigma_{\theta2}(\rho_{ti}) \\
 M_{bi} &= \sigma_{r2}(\rho_{bi}) - \nu \sigma_{\theta2}(\rho_{bi}) \\
 \mathbf{MA}_{ti} &= [\sigma_{r0}(1, \rho_{ti}, 1) - \nu \sigma_{\theta0}(1, \rho_{ti}, 1), \dots, \\ & \quad \sigma_{r0}(Max - 1, \rho_{ti}, 1) - \nu \sigma_{\theta0}(Max - 1, \rho_{ti}, 1)] \\
 \mathbf{MB}_{ti} &= [\sigma_{r1}(1, \rho_{ti}, 1) - \nu \sigma_{\theta1}(1, \rho_{ti}, 1), \dots, \\ & \quad \sigma_{r1}(Max - 1, \rho_{ti}, 1) - \nu \sigma_{\theta1}(Max - 1, \rho_{ti}, 1)] \\
 \mathbf{MA}_{ti}^* &= [\sigma_{r0}^*(1, \rho_{ti}, 1) - \nu \sigma_{\theta0}^*(1, \rho_{ti}, 1), \dots, \\ & \quad \sigma_{r0}^*(Max, \rho_{ti}, 1) - \nu \sigma_{\theta0}^*(Max, \rho_{ti}, 1)] \\
 \mathbf{MB}_{ti}^* &= [\sigma_{r1}^*(1, \rho_{ti}, 1) - \nu \sigma_{\theta1}^*(1, \rho_{ti}, 1), \dots, \\ & \quad \sigma_{r1}^*(Max, \rho_{ti}, 1) - \nu \sigma_{\theta1}^*(Max, \rho_{ti}, 1)] \\
 \mathbf{MA}_{bj} &= [\sigma_{r0}(1, \rho_{bj}, -1) - \nu \sigma_{\theta0}(1, \rho_{bj}, -1), \dots,
 \end{aligned}$$

$$\begin{aligned} & \sigma_{r0}(Max - 1, \rho_{bj}, -1) - v\sigma_{\theta0}(Max - 1, \rho_{bj}, -1) \\ \mathbf{MB}_{bj} &= [\sigma_{r1}(1, \rho_{bj}, -1) - v\sigma_{\theta1}(1, \rho_{bj}, -1), \dots, \\ & \sigma_{r1}(Max - 1, \rho_{bj}, -1) - v\sigma_{\theta1}(Max - 1, \rho_{bj}, -1)] \\ \mathbf{MA}_{bj}^* &= [\sigma_{r0}^*(1, \rho_{bj}, -1) - v\sigma_{\theta0}^*(1, \rho_{bj}, -1), \dots, \\ & \sigma_{r0}^*(Max, \rho_{bj}, -1) - v\sigma_{\theta0}^*(Max, \rho_{bj}, -1)] \\ \mathbf{MB}_{bj}^* &= [\sigma_{r1}^*(1, \rho_{bj}, -1) - v\sigma_{\theta1}^*(1, \rho_{bj}, -1), \dots, \\ & \sigma_{r1}^*(Max, \rho_{bj}, -1) - v\sigma_{\theta1}^*(Max, \rho_{bj}, -1)] \end{aligned}$$

References

- [1] K.S. Kim, H.T. Hahn, Residual stress development during processing of graphite/epoxy composites, *Compos. Sci. Technol.* 36 (2) (1989) 121–132.
- [2] H. Jiao, X.L. Zhao, Imperfection, residual stress and yield slenderness limit of very high strength (VHS) circular steel tubes, *J. Constr. Steel Res.* 59 (2) (2003) 233–249.
- [3] X. Huang, Z. Liu, H. Xie, Recent progress in residual stress measurement techniques, *Acta Mech. Solida Sin.* 26 (6) (2013) 570–583.
- [4] A. Díaz, I.I. Cuesta, J.M. Alegre, A.M.P. de Jesus, J.M. Manso, Residual stresses in cold-formed steel members: Review of measurement methods and numerical modelling, *Thin-Walled Struct.* 159 (357) (2021) 107335.
- [5] N.S. Rossini, K.Y. Dassisi, A.G. Benyounis, A.G. Olabi, Methods of measuring residual stresses in components, *Mater. Des.* 35 (2012) 572–588.
- [6] X.Z. Zhang, S. Liu, M.S. Zhao, S.P. Chiew, Comparative experimental study of hot-formed, hot-finished and cold-formed rectangular hollow sections, *Case Stud. Struct. Eng.* 6 (2016) 115–129.
- [7] L.R. Lothhammer, M.R. Viotti, A. Albertazzi, C.L.N. Veiga, Residual stress measurements in steel pipes using DSPI and the hole-drilling technique, *Int. J. Press. Vessels Pip.* 152 (2017) 46–55.
- [8] M. Beghini, L. Bertini, Recent advances in the hole drilling method for residual stress measurement, *J. Mater. Eng. Perform.* 7 (2) (1998) 163–172.
- [9] ASTM E837-13a, Standard Test Method for Determining Residual Stresses by the Hole-Drilling Strain-Gage Method, 2013.
- [10] D. Peral, J. de Vicente, J.A. Porro, J.L. Ocaña, Uncertainty analysis for non-uniform residual stresses determined by the hole drilling strain gauge method, *Measurement* 97 (2017) 51–63.
- [11] J. Guo, H.Y. Fu, B. Pan, R.K. Kang, Recent progress of residual stress measurement methods: A review, *Chin. J. Aeronaut.* 34 (2) (2021) 54–78.
- [12] N. Tebedge, G. Alpsten, L. Tall, Residual-stress measurement by the sectioning method, *Exp. Mech.* 13 (2) (1973) 88–96.
- [13] W.M. Quach, B. Young, Material properties of cold-formed and hot-finished elliptical hollow sections, *Adv. Struct. Eng.* 18 (7) (2015) 1101–1114.
- [14] B. Somodi, B. Kövesdi, Residual stress measurements on cold-formed HSS hollow section columns, *J. Constr. Steel Res.* 128 (2017) 706–720.
- [15] Y. Nakayama, T. Takaai, S. Kimura, Evaluation of surface residual stresses in cold rolled 5083 aluminum alloy by X-ray method, *Mater. Trans. JIM* 34 (6) (1993) 496–503.
- [16] C. Bouffieux, R. Pesci, R. Boman, N. Caillet, J.P. Ponthot, A.M. Habraken, Comparison of residual stresses on long rolled profiles measured by X-ray diffraction, ring core and the sectioning methods and simulated by FE method, *Thin-Walled Struct.* 104 (2016) 126–134.
- [17] F. Wang, J. Yang, I. Azim, L. Bai, Y. Ma, Experimental and numerical evaluations of the distribution and effect of roll-forming residual stress on CFS sigma beams, *J. Constr. Steel Res.* 167 (2020) 105978.
- [18] S. Caporali, G. Pratesi, S. Kabra, F. Grazzi, Type I and type II residual stress in iron meteorites determined by neutron diffraction measurements, *Planet. Space Sci.* 153 (1) (2018) 72–78.
- [19] M. Jandera, L. Gardner, J. Machacek, Residual stresses in cold-rolled stainless steel hollow sections, *J. Constr. Steel Res.* 64 (11) (2008) 1255–1263.
- [20] L. Tong, G. Hou, Y. Chen, F. Zhou, K. Shen, A. Yang, Experimental investigation on longitudinal residual stresses for cold-formed thick-walled square hollow sections, *J. Constr. Steel Res.* 73 (2012) 105–116.
- [21] Y. Ju, D. Xing, L. Mao, Z. Ren, F.-p. Chiang, Optical measurement, characterization and quantification for plastic deformations and stress in three-dimensional structures: Recent developments, challenges, and prospects, *Measurement* 186 (2021) 110212.
- [22] V.S. Pisarev, V.V. Balalov, V.S. Aistov, M.M. Bondarenko, Y.M. G., Reflection hologram interferometry combined with hole drilling technique as an effective tool for residual stresses investigation in thin-walled structures, *Opt. Laser Eng.* 36 (6) (2001) 551–597.
- [23] V.S. Pisarev, M.M. Balalov, A.N. Chernov, A.N. Vinogradova, Y.M. G., General approach to residual stresses determination in thin-walled structures by combining the hole drilling method and reflection hologram interferometry, *Int. J. Mech. Sci.* 47 (9) (2005) 1350–1376.
- [24] M. Steinzig, E. Ponslet, Residual stress measurement using the hole drilling method and laser speckle interferometry: part 1, *Exp. Tech.* 27 (3) (2003) 43–46.
- [25] G.S. Schajer, M. Steinzig, Full-field calculation of hole drilling residual stresses from electronic speckle pattern interferometry data, *Exp. Mech.* 45 (6) (2005) 526–532.
- [26] G. Rebergue, B. Blaysat, H. Chanal, E. Duc, In-situ measurement of machining part deflection with Digital Image Correlation, *Measurement* 187 (2022) 110301.
- [27] O. Yuksel, I. Baran, N. Ersoy, R. Akkerman, Investigation of transverse residual stresses in a thick pultruded composite using digital image correlation with hole drilling, *Compos. Struct.* 223 (2019) 110954.
- [28] X. Xu, S. Yong, Q. Zhang, Theoretical estimation of systematic errors in local deformation measurements using digital image correlation, *Opt. Laser Eng.* 88 (2017) 265–279.
- [29] A.E. Green, Three-dimensional stress systems in isotropic plates. I, *Philos. Trans. R. Soc. Lond. A Math. Phys. Eng. Sci.* 240 (825) (1948) 561–597.
- [30] L. Hacini, N. Van Lê, P. Bocher, Evaluation of residual stresses induced by robotized hammer peening by the contour method, *Exp. Mech.* 49 (2009) 775–783.
- [31] C. Karataş, S. Adnan, E. Dulek, Modelling of residual stresses in the shot peened material C-1020 by artificial neural network, *Expert Syst. Appl.* 36 (2009) 3514–3521.